

Optimizing Stiffness of a Novel Parallel-Actuated Robotic Shoulder Exoskeleton for a Desired Task or Workspace

Justin Hunt*, Panagiotis Artemiadis *IEEE Senior Member*, and Hyunglae Lee *IEEE Member*

Abstract— The purpose of this work is to optimize the stiffness of a novel parallel-actuated robotic exoskeleton designed to offer a large workspace. This is done in an effort to help provide a solution to the issue wearable parallel actuated robots face regarding a tradeoff between stiffness and workspace. Presented in the form of a shoulder exoskeleton, the device demonstrates a new parallel architecture that can be used for wearable hip, ankle and wrist robots as well. The stiffness of the architecture is dependent on the placement of its actuated substructures. Therefore, it is desirable to place these substructures effectively so as to maximize dynamic performance for any application. In this work, an analytical stiffness model of the device is created and validated experimentally. The model is then used, along with a method of bounded nonlinear multi-objective optimization to configure the parallel actuators so as to maximize stiffness for the entire workspace. Furthermore, it is shown how to use the same technique to optimize the device for a particular task, such as lifting in the sagittal plane.

I. INTRODUCTION

In the field of exoskeleton robotics, the close-loop architecture of parallel manipulation offers many advantages over open-loop serial chain manipulation. While the comparatively simple kinematics and large workspace of the serial manipulator gave rise to its popularity, the parallel manipulator offers low end-effector inertia, high acceleration, high position accuracy, and the potential for high stiffness [1-3]. In addition, certain parallel manipulators such as the 3-SPS (spherical-prismatic-spherical) [4] and 3-RRR (revolute-revolute-revolute) [5] designs can operate without occupying their center of rotation, which is particularly useful when interfacing with biological joints such as the shoulder, hip, wrist and ankle with multiple degrees-of-freedom (DoF).

Parallel manipulators have been used before for several different exoskeleton applications. Prior works include wearable wrist [6], ankle [7] and shoulder [8] devices. All of these demonstrate different types of parallel architecture. The RiceWrist [6] uses a 3-RPS (revolute-prismatic-spherical) manipulator with an additional serial revolute joint to generate 4-DoF. These DoF include the rotation of the forearm, wrist height and 2-DoF in rotation of the end-effector platform. The Anklebot [7] uses a 2-SPS-1S (spherical-prismatic-spherical, spherical) manipulator that consists of spherical joints and prismatic actuation in conjunction with the biological joint to achieve spherical motion. The shoulder exoskeleton BONES [8] uses a RRRS

(revolute-revolute-prismatic-spherical) manipulator to decouple and control three rotational DoF. Because all of these architectures, along with the previously mentioned 3-SPS and 3-RRR, generate spherical motion through parallel actuation, they can further be categorized as spherical parallel manipulators.

Spherical parallel manipulators (SPMs) typically offer a larger workspace than higher DoF parallel architectures [9, 10]. This is because they require fewer actuated substructures and therefore experience less mechanical interference between substructures. However, this also means they have fewer active DoF, which normally results in a drop in stiffness performance [11-13]. This can be problematic, particularly for augmentative exoskeleton systems, which must maintain rigidity under heavy loading in order to function effectively.

In an effort to improve the workspace/stiffness tradeoff of SPMs, the authors have introduced a new method of parallel architecture design in previous work [14]. The presented method involves coupling specific motions of each independent parallel substructure in order to increase the number of active DoF, which works to both constrain the kinematics and increase stiffness of the entire structure. This method was demonstrated by applying it to the design of a novel shoulder exoskeleton. Both the kinematics and workspace of the prototype developed were solved and experimentally verified in previous work [14].

One advantage of the new parallel architecture introduced in [14] is the flexibility of actuator placement. The three substructures that comprise the device can be placed in any position about a center point. Choosing this placement is critical, as the stiffness of the device was found to be highly dependent on the configuration of these substructures. For this reason, it is desirable to place these substructures effectively so as to maximize dynamic performance. Optimization techniques can be employed to maximize stiffness across an entire workspace or even for particular task, such as lifting in the sagittal plane.

The development of a stiffness optimization model would not only allow the stiffness of the shoulder exoskeleton to be maximized for a desired task or workspace, but it would also allow the architecture to be optimized for other joints as well. For example, this could include stair climbing for a hip device or running for an ankle device. Because of the significance that such a tool would have on the potential application of the novel parallel architecture described, this optimization problem is the focus of this work.

The rest of this paper presents the steps taken to optimize the stiffness of the exoskeleton shoulder for a desired task or workspace. The sections are organized as follows: Section II provides (1) a brief overview of the shoulder exoskeleton design, (2) the model used to characterize stiffness, (3) the

* Address all correspondence to this author.

All authors are with School for Engineering of Matter, Transport and Energy, Arizona State University, Tempe, AZ 85287, USA {jphunt3, panagiotis.artemiadis, hyunglae.lee}@asu.edu

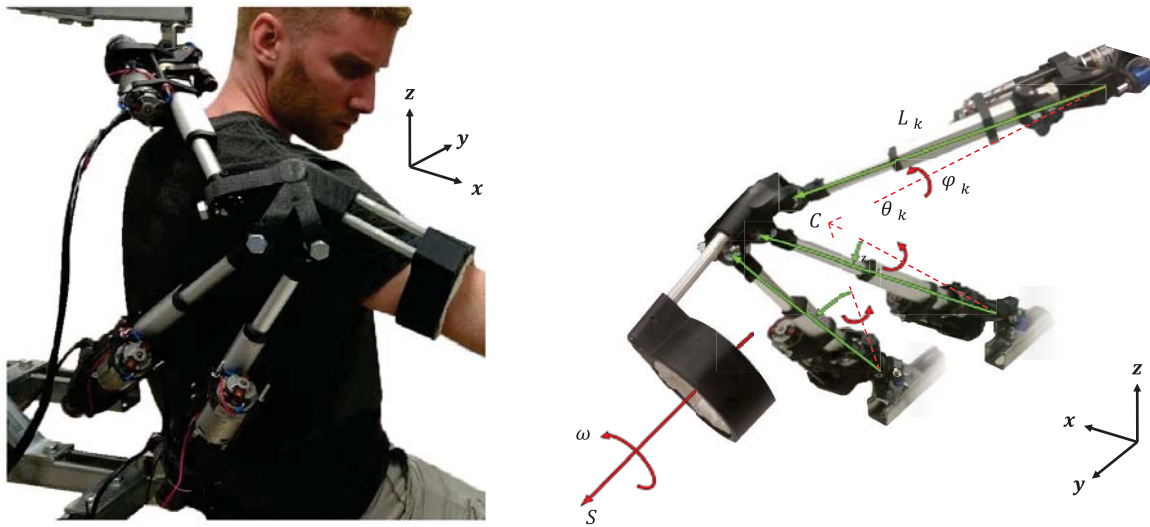


Fig. 1: Implementation of the parallel actuated wearable robotic joint in a shoulder exoskeleton application. Shown on **left** is the interface of the actual prototype with a user. Shown on **right** is the device's architecture with the active (green) and passive (red) joints illustrated. The convergence point C represents the center of rotation for all three DoF of the device's shoulder piece. The variables ω and S represent the inner cuff rotation and translation, respectively. The variables θ_k , φ_k and L_k represent the pitch, roll, and linear stroke of each actuator substructure k , respectively.

experimental setup to validate the stiffness model and (4) the optimization techniques used to maximize stiffness. Section III details (1) the results of the stiffness model validation experiment and (2) the optimal actuator placement to maximize stiffness in the sagittal plane and for an entire workspace. Finally, Section IV concludes the paper with a discussion and summary of the contribution.

II. METHODS

A. Design Overview

The developed shoulder exoskeleton is presented in Fig. 1. A simulation created to illustrate its design and operation can be found at <https://youtu.be/vm9iL-SyoS8>. The mobile shoulder piece depicted has three decoupled rotational DoF centered about the convergence point C . This point is assumed to be the center of rotation of the user's shoulder as well. However, due to possible translational motion of the user's shoulder joint, there may be an error between C and the actual center of rotation C' . To alleviate possible mechanical interference generated by the position error between C and C' , a slip mechanism is integrated into the cuff of the device. The cuff, which acts as an interface between user and device, is positioned approximately midway on the user's upper arm. The cuff consists of two concentric open cylinders. The inner cylinder is padded with compliant foam and contacts the user's arm. The outer cylinder is connected to mobile shoulder piece by aluminum tubing. When joint misalignment between the user and device occurs, the inner cylinder will translate within the outer cylinder.

The spherical motion of the shoulder piece is accomplished by using three linear actuator substructures. Each substructure k has three DoF: pitch θ_k , roll φ_k and linear stroke L_k . The pitch and linear stroke of each substructure are mechanically coupled in order to achieve an arc motion of the substructure end effector. The method of coupling is a mechanical slider geared to the linear stroke and

connected to an armature which adjusts the pitch of the actuator to a corresponding stroke length. This mechanism is detailed in Fig 2. By adjusting key variables of the motion coupling mechanism, such as slider speed and/or armature length, it is possible to adjust the radius and curvature of the substructure end effector motion. This may be necessary to avoid mechanical interference between the device and large or small users. In the current configuration, the arc is set to a constant radius of 9.5 cm. This radius was determined through measurement of the outer surface of the lateral and posterior deltoids to the approximate center of shoulder rotation of three adult male subjects. The roll of each substructure is not directly constrained, but rather set by the synergistic motion of all three substructures. Each actuated substructure is connected to the mobile shoulder piece using a 3-DoF tie rod joint.

Each actuator substructure was built using a linear actuator (FA-PO-35, Firgelli, WA). The top two actuators have a stroke length of 15.2 cm and the bottom actuator has a stroke of 10.2 cm. Each actuator was stripped of its stock motor and gearbox and modified to include a drill motor (393111-01, DeWalt, WI), custom gearbox, motion coupling mechanism, and feedback sensors. The coupled pitch angle and linear stroke length of each actuator are measured using an encoder (E6C2, Karlsson Robotics, FL) with a resolution of 1024 pulses/rotation. The roll is measured using a 10K ohm potentiometer (3590S, Bourns, CA). For testing purposes, each actuator substructure is mounted to a stationary frame. For the configuration and global frame orientation shown in Fig. 1, the Cartesian location of the top, middle and bottom mounting point with respect to C is $[-33, -10, 19]^T$ cm, $[-28, -17, -20]^T$ cm and $[-10, -12, -24]^T$ cm, respectively.

To operate the exoskeleton, a keyboard control scheme running on an off-board PC was used. A Matlab (Mathworks, MA) script was developed to map arrow keys to the elevation and azimuth of the shoulder piece. The program receives feedback from the onboard sensors via serial communication

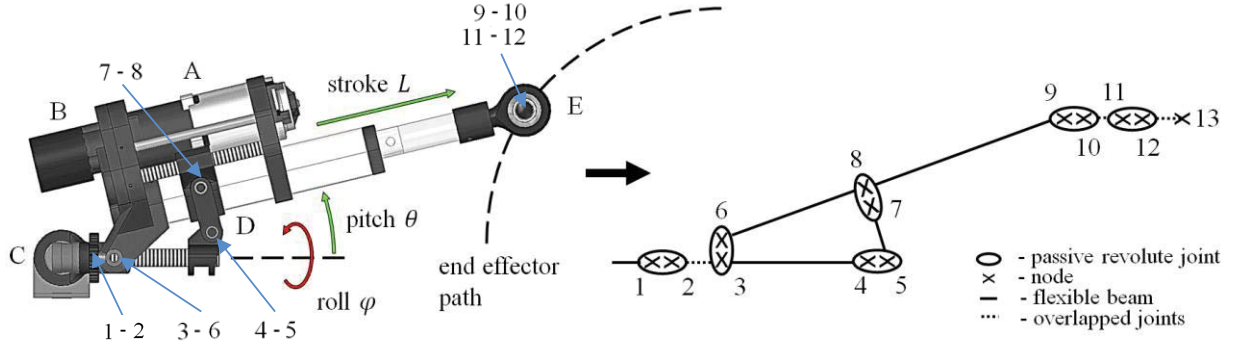


Fig. 2: Shown on left is one of the three actuated substructures with its active (green) and passive (red) DoF depicted. Key components are as follows: A) motor, B) pitch and stroke feedback encoder, C) roll feedback potentiometer, D) motion coupling mechanism with actuated slider and pitch control arm, E) 3-Dof platform mounting joint. Shown on right is the actuated substructure equivalent nodal diagram.

with a microcontroller (Mega 2560, Arduino, Italy) along with user input and uses it to solve the forward and inverse kinematics. Given an elevation and azimuth, the program determines the optimal roll angle of the shoulder piece about the user arm axis in order to keep it within the stroke length of all three actuators. Since the user does not have control over the roll angle of the shoulder, the passive cuff rotational DoF ω has been incorporated into the design in order to prevent an undesired torque from being applied to the user's arm. For a given desired shoulder orientation, actuator position and velocity commands are sent from the off-board PC through the Arduino microcontroller to a set of three PID motion controllers (0-KANGAROO2, Dimension Engineering, OH). Each PID controller is connected in loop with a 10 A motor driver (0-SYREN10, Dimension Engineering, OH).

Additional details regarding the design are provided in the prior work [14]. This reference also provides an analysis of the kinematics and workspace, which have been excluded here for brevity.

B. Stiffness Model

In order to rapidly characterize the stiffness of the shoulder exoskeleton for different mounting point configurations and end effector orientations, an analytical model was created to calculate stiffness at the center of the shoulder piece. The model was developed using a matrix structural analysis method and closely follows the work of [15]. For brevity, the reader will be referred back to this prior work for some of the more derivative or expansive steps required in the development of this model. With the model, it is possible to generate the theoretical translational and rotational stiffness ellipsoids for different configurations and orientations in order to establish a basis for comparison.

To begin, each actuated substructure k ($k = 1, 2, 3$) is deconstructed into nodes that correspond to characteristic points. Shown in Fig. 2 are the node locations for each actuator. The nodes are linked by either a flexible beam or passive revolute joint. It should be noted that beams must be modelled as flexible, since even minor beam deflections can have an impact on end effector stiffness. Each beam n is fixed at its ends by one or two nodes, depending on its

location in the substructure. Each beam is therefore represented by either a 6x6 or the 12x12 beam stiffness matrix $\mathbf{K}_{n,k}$ as defined in Euler–Bernoulli beam theory. Before these beam stiffness matrices $\mathbf{K}_{n,k}$ can be assembled into one stiffness matrix $\mathbf{K}_{T,k}$, each must be multiplied by a matrix $\mathbf{P}_{n,k}$ comprised of rotation sub matrices $\mathbf{R}_{n,k}$, which describe $\mathbf{K}_{n,k}$ with respect to the global frame. The rotation of $\mathbf{K}_{n,k}$ by $\mathbf{P}_{n,k}$ is given by

$$\mathbf{K}'_{n,k} = \mathbf{P}_{n,k}^{-1} \mathbf{K}_{n,k} \mathbf{P}_{n,k} \quad (1)$$

$$\text{where } \mathbf{P}_{n,k} = \begin{bmatrix} \mathbf{R}_{n,k} & 0 & \cdots \\ 0 & \mathbf{R}_{n,k} & \cdots \\ \vdots & \vdots & \ddots \end{bmatrix}$$

The dimension of $\mathbf{P}_{n,k}$ is determined by the dimension of $\mathbf{K}_{n,k}$. The rotated stiffness matrices $\mathbf{K}'_{n,k}$ can then be used to construct $\mathbf{K}_{T,k}$ in accordance with the stiffness matrix assembly technique described in [15-16].

The matrix $\mathbf{K}_{T,k}$ describes the stiffness of the substructure before the inclusion of the passive joints. Each passive joint is defined by a matrix $\mathbf{A}_{n,k}$ that describes the kinematic relation between adjacent nodes. To define this relation, let $\mathbf{a}_{n,k} = [a_x \ a_y \ a_z]^T_{n,k}$ be the unit vector which describes the revolute axis of a passive joint composed of two adjacent nodes. The coordinate frame of each node can be constructed using $\mathbf{a}_{n,k}$ and the axially vector $\mathbf{b}_{n,k}$ of the adjacent beam. The third coordinate frame vector, $\mathbf{c}_{n,k}$ can be determined by $\mathbf{c}_{n,k} = \mathbf{a}_{n,k} \times \mathbf{b}_{n,k}$. These coordinate frames of the two adjacent nodes can be related by a rotation about $\mathbf{a}_{n,k}$. The vectors of this rotation can be defined as:

$$\mathbf{V}_{n,k} = \begin{bmatrix} b'_x & b'_y & b'_z \\ c'_x & c'_y & c'_z \end{bmatrix}_{n,k} \quad (2)$$

The complete kinematic relation between the two nodes that describes the passive revolute joint is derived in [10] and given as:

$$\mathbf{A}_{n,k} = \begin{bmatrix} \mathbf{I}_{3 \times 3} & \mathbf{0}_{3 \times 3} \\ \mathbf{0}_{2 \times 3} & \mathbf{V}_{n,k} \end{bmatrix} \quad (3)$$

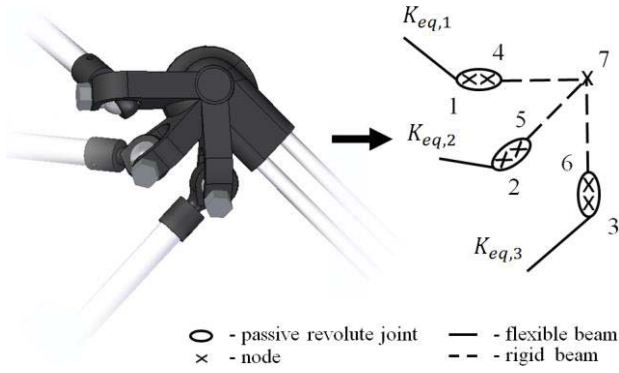


Fig. 3: Shown on left is the shoulder piece. Shown on right is the shoulder piece equivalent nodal diagram with node 7 acting as the end effector position.

The $A_{n,k}$ matrices are assembled into a single kinematic relation matrix $A_{T,k}$ in a similar manner to $K_{T,k}$. The total substructure stiffness matrix, which includes the effects of both the flexible beams and revolute joint, is derived using the minimum total potential energy principle and given as:

$$\mathbf{K}_{G,k} = \begin{bmatrix} \mathbf{K}_{T,k} & \mathbf{A}_{T,k}^T \\ \mathbf{A}_{T,k} & \mathbf{0} \end{bmatrix} \quad (4)$$

It is possible to calculate the displacement at the last node of each substructure k by permuting $\mathbf{K}_{G,k}$ in order to partition the endpoint substructure stiffness matrix $\mathbf{K}_{eq,k}$, which describes the last node. To define the stiffness of the entire structure, $\mathbf{K}_{eq,k=1,2,3}$ must be assembled to the end effector. The nodal diagram of the end effector is shown in Fig. 3. Since the shoulder piece interconnects all three substructure endpoint nodes and the end effector node, it can no longer be accurately described by Euler–Bernoulli beam theory. Instead, it will be modeled as set of rigid beams with infinite stiffness, which will require the introduction of a new kinematic relation. To start, let $\mathbf{W}_n = [L_x \ L_y \ L_z]^T$ define the vector between two nodes linked by the rigid beam. The corresponding skew-symmetric matrix of this vector is:

$$\hat{\mathbf{L}}_{W_n} = \begin{bmatrix} 0 & -L_z & L_y \\ L_z & 0 & -L_x \\ -L_y & L_x & 0 \end{bmatrix}_n \quad (5)$$

The complete kinematic relation between the two nodes that describes the rigid beam is derived in [10] and given as:

$$\mathbf{B}_n = \begin{bmatrix} \mathbf{0}_{3 \times 3} & \mathbf{I}_{3 \times 3} \\ \mathbf{I}_{3 \times 3} & \hat{\mathbf{L}}_{W_n} \end{bmatrix} \quad (6)$$

With the rigid beam defined, the kinematic relation matrix A_T of the shoulder piece is constructed. The assembly procedure for A_T is the same as it was for $A_{T,k}$, but with the inclusion of B_n . Along with A_T , the substructure stiffness matrices $\mathbf{K}_{eq,k=1,2,3}$ is assembled into a single matrix \mathbf{K}_T . The assembly technique used to construct \mathbf{K}_T is the same used for $\mathbf{K}_{T,k}$. The stiffness of the entire shoulder exoskeleton is derived by using minimum total potential energy given as:

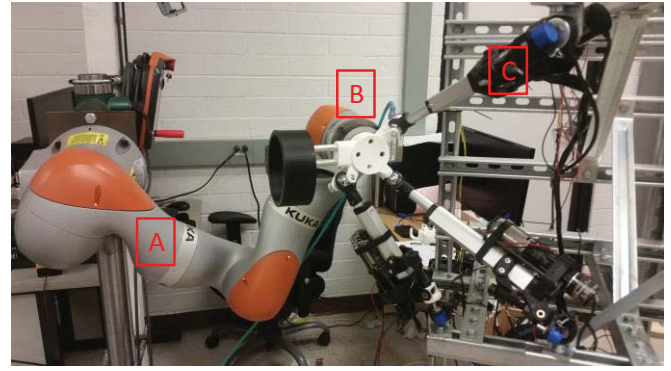


Fig. 4: Experimental setup for testing stiffness: (A) KUKA robotic arm, (B) ATI force sensor, (C) Exoskeleton shoulder.

$$\mathbf{K}_{eq,T} = \begin{bmatrix} \mathbf{K}_T & \mathbf{A}_T^T \\ \mathbf{A}_T & \mathbf{0} \end{bmatrix} \quad (7)$$

As with $\mathbf{K}_{G,k}$, it is possible to calculate the displacement at the end effector by permuting $\mathbf{K}_{eq,T}$ in order to partition the equivalent 6x6 end effector stiffness matrix \mathbf{K}_{ee} , which describes the stiffness at node 7 in Fig. 3.

The matrix \mathbf{K}_{ee} can be visualized by its translational and rotational stiffness ellipsoids. As defined in the work of [17], these ellipsoids are created by first separating \mathbf{K}_{ee} into a symmetric component \mathbf{K}_s and an antisymmetric component \mathbf{K}_a . Assume:

$$\mathbf{K}_{ee} = \begin{bmatrix} \mathbf{K}_{xx} & \mathbf{K}_{xy} \\ \mathbf{K}_{yx} & \mathbf{K}_{yy} \end{bmatrix} \quad (8)$$

Then \mathbf{K}_s and \mathbf{K}_a can be written as:

$$\mathbf{K}_s = \begin{bmatrix} \mathbf{K}_{xx} & \frac{\mathbf{K}_{xy} + \mathbf{K}_{yx}}{2} \\ \frac{\mathbf{K}_{yx} + \mathbf{K}_{xy}}{2} & \mathbf{K}_{yy} \end{bmatrix} \quad (9)$$

$$\mathbf{K}_a = \begin{bmatrix} 0 & \frac{\mathbf{K}_{xy} - \mathbf{K}_{yx}}{2} \\ \frac{\mathbf{K}_{yx} - \mathbf{K}_{xy}}{2} & 0 \end{bmatrix} \quad (10)$$

where $\mathbf{K}_{ee} = \mathbf{K}_s + \mathbf{K}_a$. The eigenvalues and eigenvectors of the symmetric component \mathbf{K}_s can now be used to represent the direction and magnitude of the translational and rotational stiffness matrices. The first three eigenvalues and three eigenvectors pairs correspond to the axes of the translational stiffness ellipsoid, while the last three correspond to the axes of the rotational stiffness ellipsoid.

C. Stiffness Model Testing

To check the results of the stiffness model, an experiment was performed to compare theoretical stiffness to that of the prototype. A 6-axis force/torque sensor (Delta IP65, ATI, NC) was coupled to the exoskeleton shoulder oriented at 90° flexion in order to measure forces and torques corresponding to displacement. To provide accurate displacement, a 7-DoF

robotic arm (LBR iiwa R820, KUKA, Germany) connected to the sensor was used. The shoulder piece used for the model and experiment has a 90° angle between tie-rod mounts, instead of the 45° angle shown in Fig. 2 and Fig. 3. This was done because early testing of the stiffness model suggested that it would produce more homogeneous stiffness ellipsoids. The experimental setup is shown in Fig. 4.

Translational displacements of 3 mm were commanded along +X, +Y and +Z. Rotational displacements of 1.5° were commanded about +X, +Y and +Z. Forces and torques corresponding to displacement were recorded at 1 kHz. The mean force measured over 5 s was used to calculate stiffness. These six measurements about the six DoF were chosen as they can be related by a transformation to each column of the theoretical stiffness matrix. As previously mentioned, this stiffness matrix is a function of the kinematic relation matrix A_T . The matrix A_T is very sensitive to change, so if it were not correct, then it would be expected that most, if not all six measurements to be significantly different from the theoretical model.

For the simulation, the flexible beams 3-4 and 6-9 shown in Fig. 2 were modeled as 1045 carbon steel and 2024 aluminum, respectively. The flexible beam 5-7 shown in Fig. 2 and the rigid links 4-7, 5-7 and 6-7 shown in Fig. 3 were modeled as ABS plastic. All critical dimensions used in the simulation match those of the prototype.

D. Stiffness Optimization

In order to maximize stiffness over a predetermined workspace, the placement of each actuator needs to be determined through optimization. Given that this is a bounded nonlinear multi-objective (rotation and translation) optimization problem, a genetic algorithm was implemented to determine the best actuator placement for a specified orientation. Matlab's Optimization Toolbox was used for this. The genetic algorithm function (ga) was given the stiffness ellipsoid volumes as negative values to minimize, thus maximizing the positive volumes. Maximizing the ellipsoid volumes will also promote homogenous ellipsoid solutions, since more spherical ellipsoids will contain greater volume. Possible solutions were restricted to the region $(-0.75 < X < -0.2, -0.75 < Y < -0.2, -0.75 < Z < -0.2)$ m corresponding to the reference frame shown in Fig. 1 with origin C . This region was chosen so that the actuators would be positioned behind the user at a comfortable distance.

The workspace of the shoulder piece and cuff were bounded by the octant (+X, +Y, -Z) shown in Fig.1 with origin C , which can also be defined by the three arm orientations: 90° flexion, 90° abduction, and at rest. Incremental 10° changes in inclination and azimuth of the shoulder piece across the entire workspace produces a point cloud of best solutions for each actuator base mount. The virtual center of each point cloud is taken as the generalized optimal solution for the corresponding workspace.

In addition to optimizing stiffness for the entire workspace, it is possible to optimize stiffness for a particular

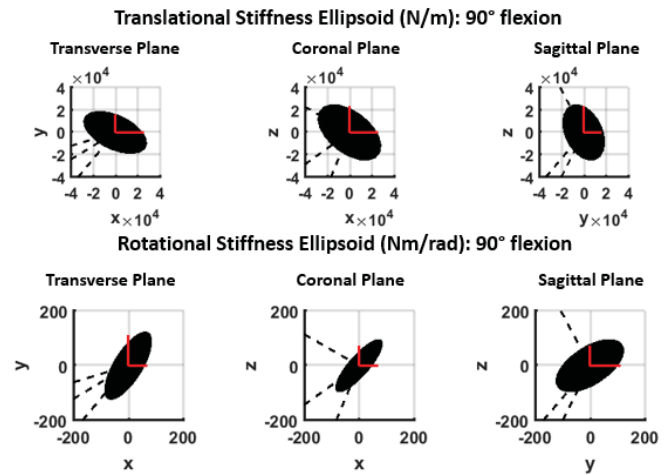


Fig. 5: Projections of the theoretical stiffness ellipsoid (black), measured axis stiffness (red) and actuator orientations for 90° flexion (dotted black).

task, such as lifting in the sagittal plane. To do this, the shoulder piece was incremented in 5° intervals between the arm at rest and 90° flexion. Similar to optimizing for the entire workspace, the point cloud of best solutions generated for each actuator are used to find the corresponding virtual centers for each actuator and thus the generalized best solution.

III. RESULTS

A. Stiffness Model Testing

A comparison of the theoretical and measured stiffness is shown in Fig. 5. For translational stiffness, the mean error along the +X, +Y, and +Z axes is 6.24% with a standard deviation of 3.79. For rotational stiffness, the mean error about +X, +Y, and +Z axes is 12.33%, with a standard deviation of 6.55. While some error does exist, it should be noted that the size and shape of the theoretical model suggests that it provides a reasonable approximation of stiffness.

The exact source of this error is unknown, however it is speculated that there are two major contributing factors, both related to the stiffness assemble matrix K_T . The first is that the model treats all components to have homogeneous elasticity and shear properties. This may not be accurate for the printed plastics used, due to the layered and honeycombed architecture inherent to 3D printing.

Second, any misalignment between the roll axis of each actuator and the center of rotation C shown in Fig. 1 will produce increased resistance to applied torque. These roll axes were positioned by hand using tooling with a tolerance of 0.5° , which may in part explain the differences seen between theoretical and experimental rotation stiffness.

B. Stiffness Optimization

For the workspace described by the octant (+X,+Y,-Z) shown in Fig.1, the actuator mounting point configuration to optimize overall stiffness is shown in Fig. 6A as a point

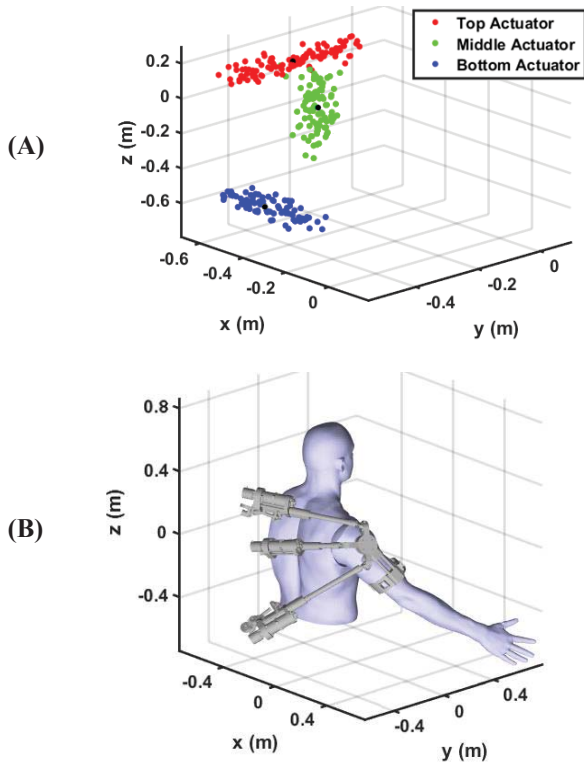


Fig. 6: (A) Point clouds representing the actuator mounting point positions corresponding to optimized stiffness for the entire workspace. Solutions are found at 10° intervals between arm at rest, 90° flexion and 90° abduction. The virtual center of each cloud is marked by a black dot. (B) Depiction of where the optimal mounting point configuration is with respect to the user. (C) Shows the generalized translational and rotational stiffness ellipsoid (black) along with the standard deviation (dotted red) for the configuration shown in Fig. 6B for movement through the entire workspace.

cloud of best solutions. These solutions were found in 10° intervals between arm at rest, 90° flexion and 90° abduction for the entire workspace. The virtual center of each point cloud for the top, middle and bottom actuator, respectively, are $A_t = [-0.5277, -0.3020, 0.1502]^T$ m, $A_m = [-0.3961, -0.3018, -0.0554]^T$ m and $A_b = [-0.3139, -0.5389, -0.4793]^T$ m. To help visualize this result, Fig. 6B shows where the optimal mounting point configuration is with respect to the user. Finally, in order to give a sense of the stiffness expected for the optimal mounting point configuration, Fig. 6C shows the corresponding generalized translational and

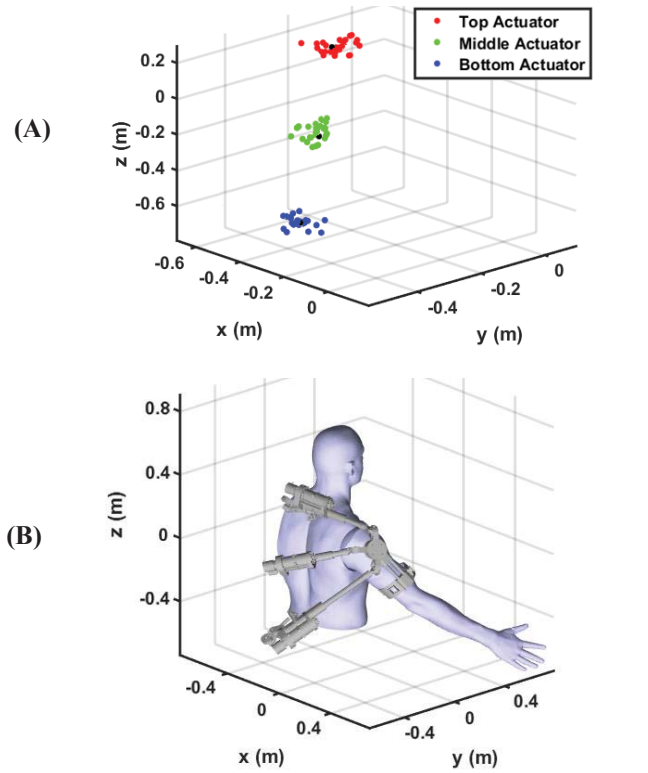


Fig. 7: (A) Point clouds representing the actuator mounting point positions corresponding to optimized stiffness for the sagittal plane. Solutions are found at 5° intervals between arm at rest and 90° flexion. The virtual center of each cloud is marked by a black dot (B) Depiction of where the mounting point configuration is with respect to the user. (C) Shows the generalized translational and rotational stiffness ellipsoid (black) along with the standard deviation (dotted red) for the configuration shown in Fig. 7B for movement in the sagittal plane only.

rotational stiffness ellipsoids. These ellipsoids represent the average stiffness found in 10° intervals between arm at rest, 90° flexion and 90° abduction for the entire workspace. Presented in a similar form to the previous result, the optimal solution for the sagittal plane is shown in Fig. 7A as a point cloud of best solutions. Solutions were found at 5° intervals between arm at rest and 90° flexion for the sagittal plane. The virtual center of each point cloud for the top, middle and bottom actuator, respectively, are $A_t = [-0.5183, -0.1524, 0.1581]^T$ m, $A_m = [-0.2905, -0.3831, -0.211]^T$ m and $A_b = [-0.1262, -0.5369, -0.4711]^T$ m. As before, Fig. 7B shows

where the optimal mounting point configuration is with respect to the user and Fig 7C shows the generalized stiffness ellipsoids corresponding to the point cloud of best solutions.

It should be noted that, while Fig. 6 and Fig. 7 represent the best solutions for the entire workspace and sagittal plane, respectively, they do not consider certain real world factors, such as mechanical interference. In these cases the results were somewhat fortunate, because the virtual center of each point cloud is not unreasonably close to the adjacent solution(s). Therefore, mechanical interference between the actuators will not occur for the workspace defined. However, this could change if the desired workspace or task were to change.

IV. DISCUSSION

This work presented here was motivated by the need for wearable robotic architectures that are capable of matching the workspace of a user while maintaining a high operational stiffness. Because of limitations in the stiffness or workspace of previous designs, the authors developed a novel parallel architecture specifically intended for interface with complex biological joints. Demonstrated in the form of a shoulder exoskeleton, the authors identify here the techniques needed to optimize the stiffness of the device in order to more effectively perform a desired task or operate in a given workspace.

The results of this paper detail a theoretical stiffness model for the novel parallel actuated shoulder exoskeleton presented, along with an experiment to validate the model. Errors of 6.24% and 12.33% for translational and rotational stiffness, respectively, were reported. Considering possible sources of errors in the stiffness model described in the Section III. A, the model still proved to be a reliable approximation of stiffness.

Using this model, along with a bounded nonlinear multi-objective optimization technique, it was shown how to configure the actuated substructures of the device so as to maximize stiffness in a given workspace. The workspace demonstrated here was equal to one octant of a sphere and defined by the three arm orientations: 90° flexion, 90° abduction, and at rest. In a similar manner, it was also shown how to maximize stiffness for certain motions within this workspace. This was demonstrated by maximizing stiffness in the sagittal plane for a lifting task. Both the results for the entire workspace and sagittal plane provided reasonable solutions with respect to real world concerns, such as mechanical interference.

The main contribution of this work is in the detailing of how the stiffness model of a novel parallel actuated shoulder exoskeleton can be used, along with optimization techniques, to maximize the device's stiffness for a particular task or workspace. Additionally, because the architecture of the device can be applied to other spherical joints like the hip, wrist and ankle, it means the stiffness model can be applied to these joints as well. Therefore, future exoskeletons using this architecture could have the stiffness of many joints

optimized for overall performance or for specific tasks, such as lifting, stair climbing or running.

REFERENCES

- [1] J.-P. Merlet, *Parallel robots* vol. 74: Springer Science & Business Media, Sophia-Antipolis, France, 2012.
- [2] H. D. Taghirad, *Parallel robots: mechanics and control*: CRC press, Boca Raton, Florida, 2013.
- [3] Y. Li and G. M. Bone, "Are parallel manipulators more energy efficient?," in *Computational Intelligence in Robotics and Automation, 2001. Proceedings 2001 IEEE International Symposium on*, 2001, pp. 41-46.
- [4] Alici, Gürsel, and Bijan Shirinzadeh. "Topology optimisation and singularity analysis of a 3-SPS parallel manipulator with a passive constraining spherical joint." *Mechanism and Machine Theory* 39.2 (2004): 215-235.
- [5] Wu, Jun, Jinsong Wang, and Zheng You. "A comparison study on the dynamics of planar 3-DOF 4-RRR, 3-RRR and 2-RRR parallel manipulators." *Robotics and computer-integrated manufacturing* 27.1 (2011): 150-156.
- [6] A. Gupta, M. K. O'Malley, V. Patoglu, and C. Burgar, "Design, control and performance of RiceWrist: A force feedback wrist exoskeleton for rehabilitation and training," *The International Journal of Robotics Research*, vol. 27, pp. 233-251, 2008.
- [7] Roy, Anindo, et al. "Robot-aided neurorehabilitation: a novel robot for ankle rehabilitation." *IEEE transactions on robotics* 25.3 (2009): 569-582.
- [8] J. Klein, S. Spencer, J. Allington, J. E. Bobrow, and D. J. Reinkensmeyer, "Optimization of a parallel shoulder mechanism to achieve a high-force, low-mass, robotic-arm exoskeleton," *IEEE Transactions on Robotics*, vol. 26, pp. 710-715, 2010.
- [9] D. R. Walter, M. L. Husty, and M. Pfürner, "A complete kinematic analysis of the SNU 3-UPU parallel robot," *Contemporary Mathematics*, vol. 496, p. 331, 2009.
- [10] Gosselin, C. M., and Jorge Angeles. "The optimum kinematic design of a spherical three-degree-of-freedom parallel manipulator." *Journal of mechanisms, transmissions, and automation in design* 111.2 (1989): 202-207.
- [11] Q. Jiang and C. M. Gosselin, "Determination of the maximal singularity-free orientation workspace for the Gough-Stewart platform," *Mechanism and Machine Theory*, vol. 44, pp. 1281-1293, 2009.
- [12] Gosselin, Clement. "Stiffness mapping for parallel manipulators." *IEEE Transactions on Robotics and Automation* 6.3 (1990): 377-382.
- [13] El-Khasawneh, Bashar S., and Placid M. Ferreira. "Computation of stiffness and stiffness bounds for parallel link manipulators." *International Journal of Machine Tools and Manufacture* 39.2 (1999): 321-342.
- [14] Hunt, Justin, Hyunglae Lee, and Panagiotis Artemiadis. "A novel shoulder exoskeleton robot using parallel actuation and a passive slip interface." *Journal of Mechanisms and Robotics* 9.1 (2017): 011002..
- [15] D. Deblaise, X. Hernot, and P. Maurine, "A systematic analytical method for PKM stiffness matrix calculation," in *Proceedings 2006 IEEE International Conference on Robotics and Automation, 2006. ICRA 2006.*, 2006, pp. 4213-4219.
- [16] Hughes, Thomas JR. *The finite element method: linear static and dynamic finite element analysis*. Courier Corporation, 2012.
- [17] F. A. Mussa-Ivaldi, N. Hogan, and E. Bizzi, "Neural, mechanical, and geometric factors subserving arm posture in humans," *The Journal of neuroscience*, vol. 5, pp. 2732-2743, 1985.